PERGAMON

International Journal of Solids and Structures 38 (2001) 6241–6264

INTERNATIONAL JOURNAL OF SOLIDS and STRUCTURES

www.elsevier.com/locate/ijsolstr

Numerical simulation of plugging failure in ballistic penetration

T. Børvik *, O.S. Hopperstad, T. Berstad, M. Langseth

Structural Impact Laboratory (SIMLab), Department of Structural Engineering, Norwegian University of Science and Technology, N-7491 Trondheim, Norway

Received 8 October 1999

Abstract

A coupled computational material model of viscoplasticity and ductile damage has been developed and implemented in LS-DYNA. This model gives good agreement between numerical simulations and experimental observations of plugging failure in ballistic penetration, without the use of inverse modelling or predefined defects. However, even if the model constants can be determined from relatively simple uniaxial tensile tests, the computational model is rather comprehensive. In this paper numerical results obtained by using the fully coupled computational model are compared with results obtained from less sophisticated versions of the material model. The differences between the numerical results will be pointed out and discussed, and details from some of the simulations are shown. To validate the accuracy of the computational model, references will be made to experimental observations from gas-gun penetration tests on 8-mm thick Weldox 460 E steel plates.

Keywords: Impact; Experimental results; Numerical simulations; Viscoplasticity; Damage; Failure

1. Introduction

The finite element method has been accepted as a general computational tool within most branches of industry and is nowadays used to simulate virtually all kinds of non-linear events. Nevertheless, there are still some classes of problems that are very hard to treat numerically. According to Belytschko (1996), simulations involving material instabilities and response discontinuities are among the most difficult problems to solve. One incident that falls within this class of problems is plugging failure of metal plates impacted by blunt-nosed cylindrical projectiles in the sub ordnance velocity regime. Here, the material in front of the projectile is rapidly accelerated at impact, giving a relative velocity within the target. This gives rise to localised deformation under adiabatic conditions in narrow zones at the well-defined periphery of the projectile. Damage due to growth of microcracks and microvoids, and heat generated by plastic work, develops in the shear bands. Material instability is assumed to appear if the temperature and damage

* Corresponding author. Tel.: +47-73-59-46-47; fax: +47-73-59-47-01.
E-mail address: tore.borvik@bygg.ntnu.no (T. Børvik).

0020-7683/01/$ - see front matter
PII: S0020-7683(00)00343-7

Nomenclature

ΔD	projectile nose deformation, i.e. $\Delta D = D_f - D_i$
ΔL	projectile length reduction, i.e. $\Delta L = L_i - L_f$
CPU	computational time
d	diameter
D	projectile nose diameter
El	number of removed elements
h	thickness or height
HRC	hardness Rockwell C
K	kinetic energy
L	projectile length
t	time
T	temperature
m	mass
v	velocity
W	work
w	deformation

Subscripts

bl	ballistic limit
c	cavity
f	final value or fracture
g	global part of target
i	initial value
l	local part of target
m	maximum value
p	projectile
pe	permanent value
pl	plug
r	residual value
t	target

softening overcome the strain and strain-rate hardening (Bai and Dodd, 1992). When the strain reaches a critical value, a discontinuous crack starts to grow towards the rear side of the target. A plug of material is finally punched out, leaving an almost circular hole in the target. The complexity of this fracture process has limited the use of both analytical and numerical solutions, and the problem has mostly been treated experimentally.

The first attempts of solving plugging failure numerically used simplified constitutive models together with erosion algorithms or element-kill techniques. Chen (1992) gave an example where such a method was used successfully, but the result depended on a user defined failure strain that is hard to determine through material tests. Bammann et al. (1990) pointed out that a plastic strain or similar is inadequate as a fracture criterion since the failure is highly dependent on many factors such as strain path, strain-rate, temperature and stress state. He found that only models where all these phenomena were included could be used to predict failure when complex stress states were present. Nicholas and Rajendran in Zukas (1990) came to a similar conclusion in their extensive review on the behaviour of materials under impact-generated high

strain-rate loading conditions. Due to observations like these, Bammann presented a constitutive model based on internal state variables that described deviatoric plasticity independent of void growth. The effect of void growth was then coupled to the plastic flow using a model based on micro mechanics. Using this model, close agreement was obtained between numerical simulations and experimental results of plugging failure in aluminium plates impacted by hardened steel projectiles.

In the present work, a somewhat similar approach is used. Here, a computational model based on the constitutive model and fracture strain model by Johnson and Cook (1983, 1985) is used to simulate plugging failure during ballistic penetration. In order to include material degradation due to damage, the constitutive model is coupled with ductile damage mechanics as proposed by Lemaitre (1992). That the Johnson–Cook model is able to describe material instability was demonstrated in a paper by Chou et al. (1991). They carried out controlled penetration experiments to produce adiabatic shear bands in steel plates. Simulations showed that shear bands could form without initial disturbances or defects if thermal softening in the material was accounted for. The calculated shear band lengths were in good agreement with those measured experimentally. A similar problem was investigated numerically by Batra and Peng (1996), showing similar results. Chou also discussed the importance of using a refined element mesh since the width of a shear band in steel typically is at the order of 10–100 μm (Bai and Dodd, 1992). In the bands, very large thermal and deformation gradients will be present. No mesh sensitivity on the general shape of the shear band was observed as long as the elements were sufficiently small, but an adaptive meshing technique was found favourable in order to maintain a fine mesh in the area where shear bands were formed. This is in accordance with Needleman (1988), who found that pathological mesh size effects do not occur in simulations if material rate dependency is accounted for. The possibility and effects of adiabatic shear localisation in dynamic punching tests of steel, aluminium and titanium were studied both experimentally and numerically by Roessig and Mason (1999). Experimentally they observed that in the titanium alloy, having a high strength and a low strain hardening, shear localised readily. In 1018 steel with moderate strength and strain hardening, some evidence of shear localisation was found at the highest loading rates. The deformation in the aluminium alloy did not localise in any of the tests carried out. In the numerical simulations, they used a maximum stress criterion and the Johnson–Cook model to determine the occurrence of shear localisation. It was found that the criterion for adiabatic shear localisation was satisfied in the simulation of the titanium alloy, giving a distinct drop in the equivalent stress and high local strains. The strain was more widely distributed in the other two materials, where the same criterion was not satisfied. Camacho and Ortiz (1997) modified the Johnson–Cook model slightly. They also used an adaptive meshing technique to avoid deformation-induced mesh distortions and contact problems during penetration. Simulations showed to be in good agreement with perforation tests of aluminium plates by conical-nosed projectiles if a pilot hole throughout the target thickness was modelled.

The computational model used in this study does not need predefined defects in order to describe failure, and all material parameters can be identified from standard material tests (Børvik et al., 1999b). No inverse modelling or model tuning is necessary in order to obtain good agreement with experimental results of plugging failure in metal plates. Due to the model formulation, i.e. no coupling between the different physical effects, it is possible to investigate the influence on the final results by including or omitting parameters such as damage, temperature and strain-rate in the model. First in this paper, experimental data from gas-gun penetration tests on 8-mm thick Weldox 460 E steel plates impacted by blunt-nosed projectiles is given. This data will be used to validate the numerical results. Then the main content of the computational model is given, together with model constants as obtained from material tests. Numerical simulations are carried out, and in the first set of simulations the fully coupled material model is used. The model is then simplified by omitting the different physical effects, one by one, until a quasi-static material model with a user defined failure strain remains. The differences between the numerical results will be pointed out and discussed, and references will be made to the experimental data. Details from simulations using the fully coupled computational model of viscoplasticity and ductile damage are shown to demonstrate

the capability and accuracy of the model. In this paper, only fixed element meshes are used. Simulations using adaptive meshing in order to solve the penetration problem is treated in a following paper (Børvik et al., 2000).

2. Experimental set-up and test results

An experimental study on the ballistic penetration of 8-mm thick Weldox 460 E steel plates has been carried out. In the tests, a compressed gas-gun (Børvik et al., 1998a) was used to launch the sabot mounted blunt-nosed projectiles at impact velocities just below and well above the ballistic limit, i.e. the critical plugging velocity, of the target plates. The different sabot pieces were stopped in a sabot trap prior to impact. Nominal hardness (HRC 53), diameter (20 mm), length (80 mm) and mass (0.197 kg) of the cylindrical projectiles were kept constant in all tests. The targets, having a free span diameter of 500 mm, were clamped in a circular frame. Initial and final velocities were optically measured, and the ballistic limit curve of the target was constructed. In addition, a digital high-speed camera system was used to photograph the penetration event. Based on the digital images, impact angles, perforation time and projectile velocity–time curves during penetration were determined. It is referred to Børvik et al. (1998a,b) for more details regarding the experimental set-up and measurement techniques used in the tests.

Some data from the experimental tests is given in Table 1. The difference in nominal and initial measured values was negligible. Projectile pitch and target oblique were also obtained and found to be small. From the measured initial velocities the ballistic limit of the target was estimated to 154.3 $\mathrm{m\,s^{-1}}$, given as the average between the highest projectile velocity not giving perforation and the lowest projectile velocity giving complete perforation of the target. In test 8–7 perforation did not occur, and this test was assigned for a microscopic investigation. An image of the sectioned and etched cross-section is shown in Fig. 1. Here, the projectile indentation and localised areas are clearly seen. The ballistic limit curve of the target material is given in Fig. 2(a), while Fig. 2(b) shows measured permanent deformation profiles as function of projectile impact velocity. The actual maximum deformation during penetration is found from the high-speed

Table 1
Experimental data for the 8-mm thick Weldox 460 E steel plates

Test #	v_i ($\mathrm{m\,s^{-1}}$)	v_{rp} ($\mathrm{m\,s^{-1}}$)	v_{rpl} ($\mathrm{m\,s^{-1}}$)	m_{pl} (g)	w_{tm}[a] (mm)	d_{cm}/d_{plm} (mm)	h_c (mm)	h_{pl} (mm)	ΔD (mm)	ΔL (mm)	t_f[b] (μs)
8–13	298.0	241.4	261.2	18.7	0.98	20.7/21.3	11.1	7.9	0.58	0.47	28
8–1	250.8	191.7	222.7	18.8	1.02	20.4/20.8	10.3	8.0	0.38	0.38	35
8–2	190.7	132.3	168.2	18.6	2.31	20.3/20.8	10.4	8.1	0.15	0.10	51
8–14	182.2	122.6	143.4	18.1	2.40	20.2/20.5	11.2	7.9	0.12	0.14	–
8–8	173.7	112.0	131.0	18.5	2.64	20.2/20.8	10.2	8.0	0.08	0.10	82
8–5	165.2	83.7	99.1	18.5	3.69	20.3/20.6	10.1	8.2	0.07	0.12	107
8–9	161.1	78.7	95.4	18.5	3.05	20.2/20.4	10.0	8.1	0.11	0.09	104
8–3	160.7	76.0	102.8	18.2	3.91	20.2/20.5	10.2	8.2	0.11	0.09	109
8–11	160.2	70.2	82.5	18.2	3.93	20.3/20.4	10.2	8.0	0.09	0.15	104
8–10	160.0	71.6	98.7	18.6	2.96	20.3/20.8	10.0	8.2	0.05	0.07	100
8–6	159.0	41.7	83.6	18.2	5.04	20.6/20.9	9.9	8.1	0.02	0.05	106
8–12	156.0	52.0	86.0	18.3	4.52	20.7/21.1	10.1	8.0	0.06	0.12	108
8–7	152.5	0	0	0	5.02	–/–	3.8[c]	–	0.07	0.05	–
8–4	137.4	0	0	0	4.85	–/–	2.9[c]	–	0.01	0.02	–

[a] $w_{tm} = w_{pe} - w_i$.
[b] Fracture time *estimated* from high-speed camera images.
[c] Projectile indentation.

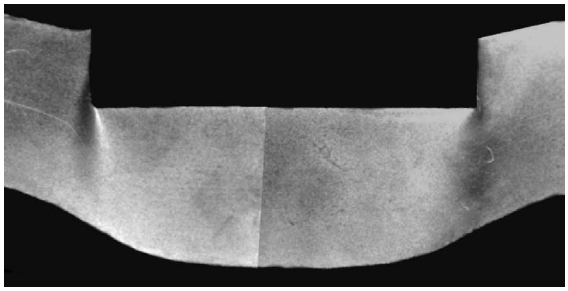

Fig. 1. Macrograph of test 8–7 showing projectile indentation and localisation.

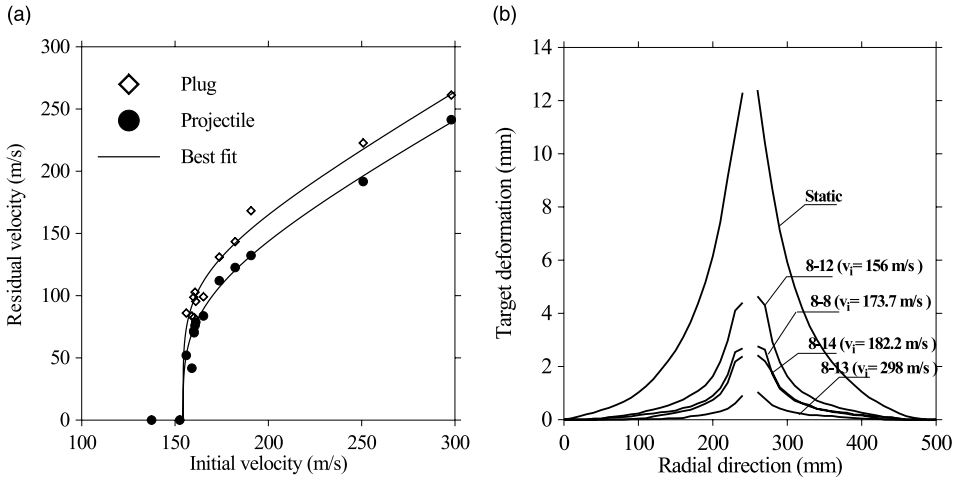

Fig. 2. (a) Ballistic limit curves and (b) measured permanent deformation profiles.

camera images to be about twice as large as the permanent one given in Fig. 2(b) and Table 1. As seen, considerable global target deformation occurs close to the ballistic limit, while the deformation is much more localised at the highest impact velocities. Fig. 3 gives measured projectile distance–time curves and calculated velocity–time curves during penetration, while some of the high-speed camera images from test 8–8 and 8–13 are shown in Fig. 10. A typical projectile and plug after the test can be seen in Fig. 12.

3. Computational model

Only the main content of the computational model of viscoplasticity and ductile damage used in the simulations is given in the following. A more detailed description can be found in Børvik et al. (1999b). The model is based on the work by Johnson and Cook (1983, 1985), Camacho and Ortiz (1997) and Lemaitre (1992), and includes linear thermoelasticity, the von Mises yield criterion, the associated flow rule, isotropic strain hardening, strain-rate hardening, softening due to adiabatic heating, softening due to isotropic damage evolution and a fracture criterion. The equivalent von Mises stress σ_{eq} is given as

$$\sigma_{eq} = [1 - \beta D]\,[A + Br^n]\,[1 + \dot{r}^*]^C\,[1 - T^{*m}] \tag{1}$$

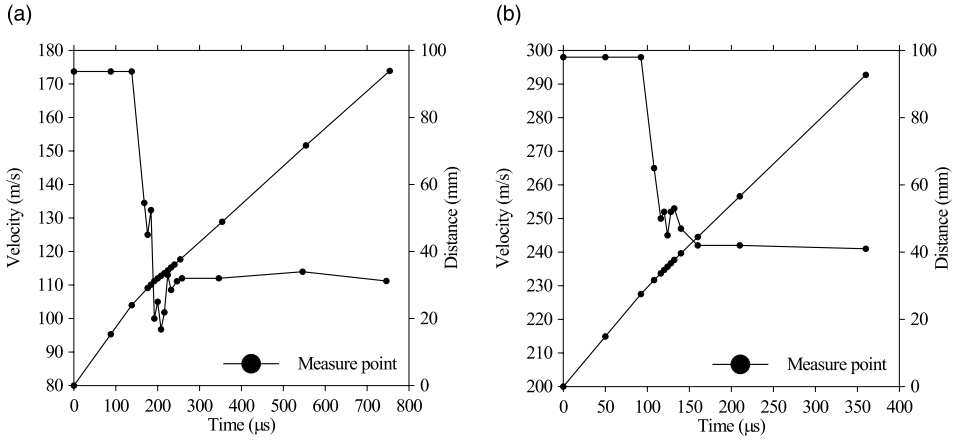

Fig. 3. Measured projectile distance–time curve and calculated velocity–time curve from test (a) 8–8 and (b) 8–13 based on the high-speed camera images.

where D is the damage variable, and β reads 0 (no damage coupling) or 1 (damage coupling); A, B, C, n and m are material constants; r is the damage accumulated plastic strain given as $\dot{r} = (1 - D)\dot{p}$, where p is the accumulated plastic strain (Lemaitre, 1992); $\dot{r}^* = \dot{r}/\dot{r}_0$ is a dimensionless strain-rate, and $\dot{r}_0$ is a reference strain-rate; $T^* = (T - T_0)/(T_m - T_0)$ is the homologous temperature, where T is the actual temperature, T_0 is the room temperature and T_m is the melting temperature of the target material, respectively. The damage variable takes values between 0 (undamaged) and 1 (fully broken). However, the critical value of damage is found to be less than 1. Hence, fracture occurs when

$$D = D_C \leqslant 1 \tag{2}$$

A damage evolution rule is proposed as

$$\dot{D} = \begin{cases} 0 & \text{when } p < p_d \\ \frac{D_C}{p_f - p_d}\,\dot{p} & \text{when } p \geqslant p_d \end{cases} \tag{3}$$

where D_C is the critical damage, $\dot{p}$ is the plastic strain-rate, p_d is the damage threshold and p_f is a fracture strain depending on stress triaxiality, strain-rate and temperature given as

$$p_f = [D_1 + D_2 \exp(D_3 \sigma^*)]\,[1 + \dot{p}^*]^{D_4}\,[1 + D_5 T^*] \tag{4}$$

where D_1–D_5 are material constants, $\sigma^* = \sigma_m/\sigma_{eq}$ is the stress triaxiality ratio and σ_m is the mean stress. The first bracket in Eq. (1) describes material degradation due to damage. The irreversible damage evolution is related to the accumulated plastic strain through Eq. (3). In the implementation, a constant β is connected to the damage variable. When β equals 1, damage is coupled to the constitutive equation. Otherwise, if β equals 0 there is no coupling with damage. The second bracket in Eq. (1) gives the strain hardening, while the effect of strain-rate hardening based on the work by Camacho and Ortiz (1997) is described in the third bracket. The last bracket in Eq. (1) gives the effect of temperature softening on the equivalent stress. The temperature increase is based on the empirical assumption that 90% of the plastic work under adiabatic conditions is dissipated as heat (Bammann et al., 1993). Any heat transfer with the surroundings is neglected in the model. When softening due to damage and temperature exceeds the strain and strain-rate hardening, localisation is assumed to occur (Bai and Dodd, 1992). The model is implemented in LS-DYNA (1999) using a fully vectorised backward-Euler integration algorithm (Berstad et al. 1994). To allow crack

growth during penetration, the model is coupled with an element-kill algorithm available in LS-DYNA that removes the damaged element from the mesh when the damage variable reaches its critical value D_C.

Four types of tensile tests are required to identify the material constants used in the model (Børvik et al., 1999b). Quasi-static tensile tests are used to identify the elastic constants E and v, and the yield stress A of the material. Notched-specimen tensile tests define the strain hardening constants B and n, the critical damage D_C, and the fracture strain constants D_1, D_2 and D_3. Dynamic tensile tests give the viscoplastic constant C and the fracture strain constant D_4. Tensile tests at elevated temperatures provide the constants m, K and D_5, defining the temperature effect on the stress–strain curve, elastic modulus and fracture strain, respectively. Quasi-static tensile tests are also carried out in order to identify the material constants for the projectile. Details regarding the material tests and calibration procedure can be found in Børvik et al. (1999b). Here, the model constants used for the target material and projectile are listed in Tables 2 and 3, respectively.

4. Numerical simulations

4.1. Numerical models

One major scope of the present work was to investigate the importance of the material model in finite element simulations of plugging failure in structural impact. This was found necessary since it is generally assumed that the details in the material relationship are crucial in the problem, especially at impact velocities close to the ballistic limit of the target material (Harding, 1989). Only the material model of the target plate was varied in the simulations, and unless otherwise stated in the text the material input was as given in Tables 2 and 3 (Børvik et al., 1999b). In order to have reliable results, the numerical simulations were validated against the experimental data given in Table 1. As demonstrated in Figs. 1 and 2(b), the 8 mm thick target plates showed a distinct combination of global deformation and localised shearing. This, together with the demand of a model for material failure as well as numerical methods for contact, fracture and crack propagation in the element grid, makes this type of simulations rather complex.

Table 2
Model constants for Weldox 460 E steel (see Børvik et al. (1999b) for notation)

Elastic constants and density			Yield stress and strain hardening			Strain-rate hardening		Damage evolution		
E (Gpa)	v	ρ (kg m^{-3})	A (MPa)	B (MPa)	n	$\dot{p}_0, \dot{r}_0$ (s^{-1})	C	β	D_c	p_d
200	0.33	7850	490	807	0.73	5×10^{-4}	0.0114	1	0.30	0

Adiabatic heating and temperature softening							Fracture strain constants				
C_p (J kg^{-1} K^{-1})	α	$\bar{\alpha}$ (K^{-1})	T_m (K)	T_0 (K)	m	K	D_1	D_2	D_3	D_4	D_5
452	0.9	1.1×10^{-5}	1800	293	0.94	0.74	0.0705	1.732	−0.54	−0.015	0

Table 3
Material constants for hardened projectile (see Børvik et al., 1999b, for notation)

E (GPa)	v	ρ (kg m^{-3})	σ_0 (MPa)	E_t (MPa)	Mean ε_f (%)
204	0.33	7850	1900	15000	2.15

The Johnson–Cook formulation has been somewhat criticised in the literature due to its empirical origin and non-coupling between physical effects, in contrast to e.g. the Zerilli and Armstrong (1987) model. However, in practical applications it has many benefits. Due to its simple form it is straightforward both to calibrate and implement the model. Also, the non-coupling between the different physical effects allows the user to add or omit complexity in the simulations using the same material model. In this study, eight different versions of the material model given by Eqs. (1)–(4) were used. These are presented in Table 4, where "x" indicates that the effect is included in the simulation. Note that the model constants B, n and D_c in Table 2 were determined simultaneously from notched specimen tensile tests (Børvik et al., 1999b). If softening due to damage is neglected in the computational model ($\beta = 0$), the hardening coefficients B and n becomes 561 MPa and 0.65, respectively, determined from smooth specimen tensile tests. Here, no Bridgman correction to the average axial stress to compensate for the introduction of transversal stresses in the necked region was carried out. A possible method to correct for the triaxial stresses in the neck of a smooth specimen has been given by Le Roy et al. (1981). If this approach is used, B and n become 383 MPa and 0.45, respectively.

In Table 4, M1 represents a fully coupled damage model, while M6 describes a simple quasi-static material behaviour with an assumed constant failure strain of 0.8. The other models describe a material behaviour in between these two extremes. The failure strain in M6 is adopted from a paper by Wen and Jones (1996), while the failure strain of 1.6 used in M5 and M7 is close to the true strain at fracture measured in a smooth quasi-static tensile test (Børvik et al., 1999b). M8 is identical to M1, except that M8 includes thermoelasticity. This involves an extra term in the deformation rate tensor, and a linear reduction in elastic stiffness with temperature (Børvik et al., 1999b). Calculated true stress–strain curves for the target using the material input in Tables 2 and 4 are shown in Fig. 4. Here, σ^* is assumed constant and equal to $1/3$ (i.e. smooth specimen), while $\dot{p}$ is constant and equal to 1000 s^{-1} (assumed adiabatic conditions). The differences between the different material models used are as seen considerable.

Earlier simulations have indicated the problem to be mesh size sensitive due to the localisation of deformation (Hopperstad et al., 1998). This effect was however not found pathological since the result converged monotonically towards a limit solution when the element size was sufficiently reduced (Børvik et al., 1999b). The mesh dependence is in fact expected since the width of the localised shear zone obtained experimentally is much smaller than the element size normally used (see e.g. Fig. 1). In order to check the mesh sensitivity, two different mesh densities were applied in the simulations. The element size in the coarse mesh was 0.5×0.4 mm^2 in the impact region, giving 20 elements over the target thickness. In the refined mesh the smallest elements were 0.125×0.1 mm^2, giving 80 elements over the target thickness. The meshes were somewhat refined towards the centre, but no adaptive remeshing technique has been applied in

Table 4
Computational models used in the simulations

Model #	Constitutive model				Fracture strain model		
	Damage	Temperature	Strain-rate	Hardening	Triaxiality	Strain-rate	Temperature
M1	x	x	x	x	x	x	$D_5 = 0$
M2	$\beta = 0$	x	x	x	x	x	$D_5 = 0$
M3	$\beta = 0$	$\alpha = 0$	x	x	x	x	$D_5 = 0$
M4	$\beta = 0$	$\alpha = 0$	$c = 0$	x	x	$D_4 = 0$	$D_5 = 0$
M5	$\beta = 0$	$\alpha = 0$	$c = 0$	x	$D_1 = 1.6$[a]	$D_4 = 0$	$D_5 = 0$
M6	$\beta = 0$	$\alpha = 0$	$c = 0$	x	$D_1 = 0.8$[a]	$D_4 = 0$	$D_5 = 0$
M7	$\beta = 0$	x	x	x	$D_1 = 1.6$[a]	$D_4 = 0$	$D_5 = 0$
M8[b]	x	x	x	x	x	x	$D_5 = 0$

[a] $D_2 = D_3 = 0$.
[b] Thermoelasticity included.

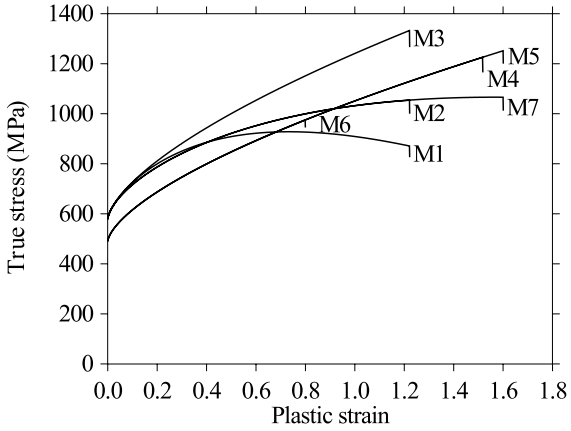

Fig. 4. Calculated stress–strain curves showing the different material models.

this study. Therefore, the axisymmetric finite element meshes used in the LS-DYNA (1999) simulations consisted of either 3120 or 20560 four-node 2-D elements with one integration point. The target was modelled using the material model defined by Eqs. (1)–(4) and the material input in Tables 2 and 4, while the projectile of hardened tool steel was modelled as elastoplastic with the material constants in Table 3. In the simulations, the plate was fully clamped at the support, while the projectile was given an initial velocity. Contact between the projectile and target was modelled using an automatic 2-D penalty formulation without friction. Frictional effects are assumed of minor importance in this particular problem (Zukas, 1990). Owing to the CPU requirement, the analyses were stopped before the elastic rebound of the target plate was completed. Hence, the final target deformation as given in Fig. 2(b) was not obtained. All simulations were carried out on a HP C360 workstation.

4.2. Coarse element mesh

Projectile residual velocities using the coarse element mesh are compared with the experimental data in Fig. 5(a), while numerical details from these simulations can be found in Børvik et al. (1999c). The ballistic limits obtained using the different models are given in Table 5. These values and the solid lines through the data points in Fig. 5 were estimated based on an analytical model proposed by Recht and Ipson (1963)

$$v_r = a\left(v_i^p - v_{bl}^p\right)^{1/p} \tag{5}$$

The method of least squares was used to fit the model constants a, p and v_{bl} to the simulated residual projectile velocities (see Table 5). This approach has earlier given accurate results (Børvik et al., 1999a). As seen, none of the models were able to predict the experimentally obtained ballistic limit within 30%. However, at impact velocities well above the ballistic limit, all models showed reasonable agreement with the experiment results. Thus, the difference between the computational models seems to increase as the impact velocity approaches the experimentally obtained ballistic limit. Keep in mind that the ballistic limit velocity is the parameter searched for in practical application. Strain-rate and temperature were both found to be important parameters. If not included in the model as in M3, M4 and M6, considerable errors appeared. A constant failure strain was also found to be a poor choice for a failure criterion when the details in the simulations were considered. However, the estimated ballistic limits for M5 and M7 were found to be in relatively close agreement with M1 and M2, where the effect of triaxiality on the failure strain was included. M5, which is a simple quasi-static model with a constant failure strain of 1.6, showed a surprisingly

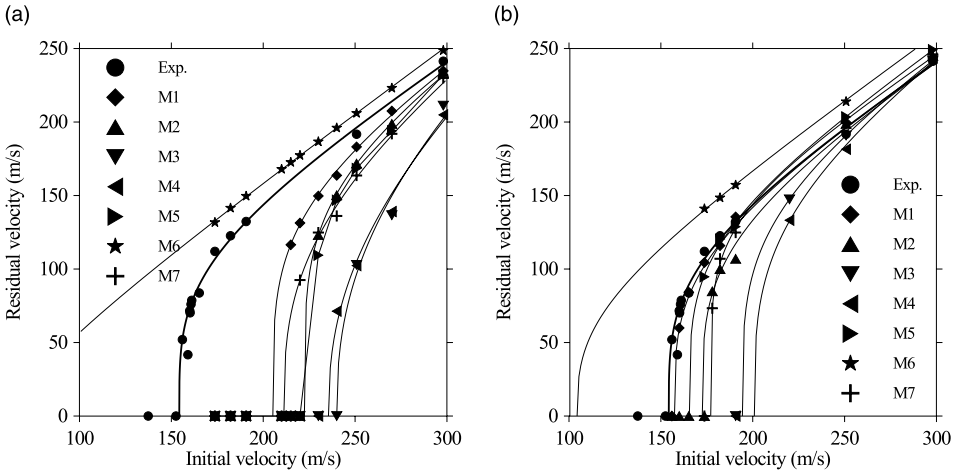

Fig. 5. Comparison between experimental and numerical ballistic limit curves using (a) a coarse element mesh and (b) a fine element mesh.

Table 5
Estimated ballistic limits using the coarse or refined element mesh

	Experiment	M1	M2	M3	M4	M5	M6	M7
Coarse mesh								
v_{bl} (m s^{-1})	154.3	205.3	222.4	240	235.5	224.8	64.7	211.2
p	3.59	4.06	4.42	2.45	2.38	4.17	1.56	2.92
a	0.83	0.84	0.84	0.97	0.96	0.85	0.89	0.89
Fine mesh								
v_{bl} (m s^{-1})	154.3	157.4	172.5	194.4	200.9	165.5	104.4	177.1
p	3.59	3.54	3.71	3.92	3.46	3.95	2.90	5.28
a	0.83	0.83	0.84	0.86	0.88	0.86	0.88	0.83

close agreement with M2, which can be considered as the original Johnson–Cook fracture model (1985). This accordance is assumed to be a coincidence. The difference between M1 and M8, i.e. the effect of including thermoelasticity in the simulations, was found to be small in all simulations. Thus, the effect of thermoelasticity in the material model is assumed negligible in this velocity regime.

Due to the findings described above, only M1, M2 and M7 were considered in any detail. The coupled computational model of viscoplasticity and ductile damage (M1) showed the closest agreement with the experimental results, but the difference in ballistic limit between M1, M2 and M7 was not significant (see Table 5). However, when the details in the numerical simulations were compared, important and distinct differences were obtained. The details revealed that M1 gave the highest local temperature, the smallest global deformation and a more confined plastic strain distribution, indicating a better description of the localisation. It also gave the lowest perforation time, which made M1 more efficient regarding CPU time than both M2 and M7. Based on the numerical data, a rough energy balance was established. This was possible since the target material was modelled as one local and one global part with identical properties. The border between the two parts was placed 0.5 mm outside the projectile boundary (see Fig. 6). The amount of energy absorbed by the different parts at the computational termination time using the coarse element mesh is shown in Fig. 7(a). Close to the ballistic limit, 60% of the energy was absorbed in the global

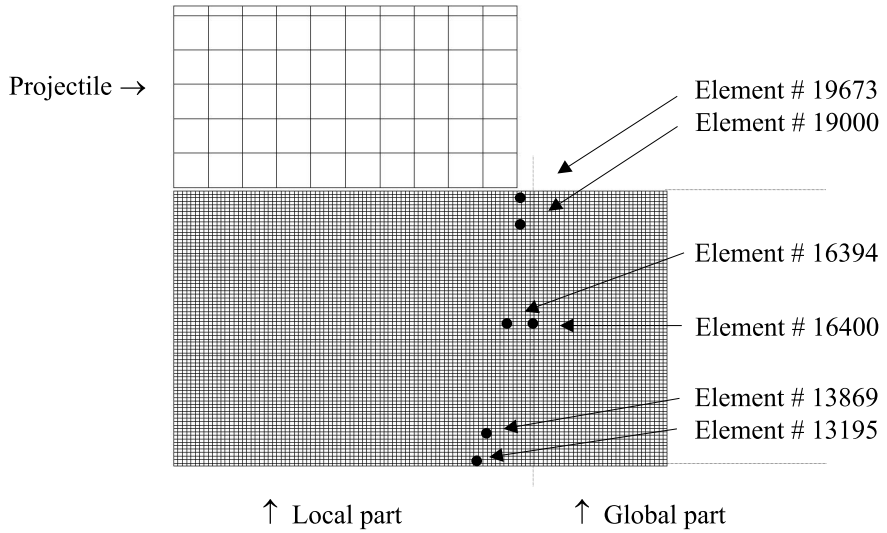

Fig. 6. Details from the element mesh showing the different parts in the simulations.

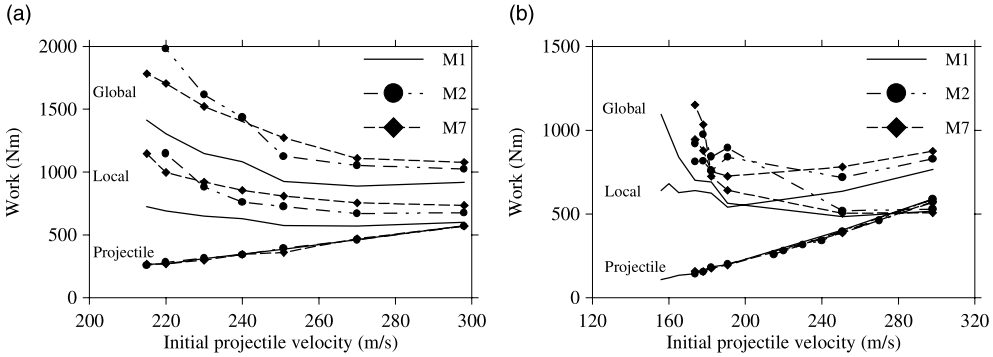

Fig. 7. Energy absorbed in the different parts during impact with (a) coarse element mesh and (b) fine element mesh.

part, 30% in the local part and 10% in projectile deformation. At the highest impact velocities, approximately 45% of the energy was absorbed globally, 30% locally and 25% by the projectile. The target absorbed less energy at all velocities using M1. It was also found that 4–5% of the total energy was lost in the simulations, mainly due to internal energy in removed elements. However, in the latest version of LS-DYNA the internal energy of removed elements and the kinetic energy of eroded nodes are stored and may therefore be included in the total energy balance. The effect of energy and mass losses in simulations using an element erosion technique was studied in detail by Børvik et al. (2000). It was found that conservation of both energy and mass was fulfilled if number of eroded elements and nodes were moderate.

4.3. Fine element mesh

Residual velocities of the projectile using the fine element mesh are compared with the experimental data in Fig. 5(b), while numerical details from some of the runs can be found in Table 6. Two major differences

Table 6
Numerical results using 80 elements over the target thickness (refined mesh)

Run #	v_r ($m\,s^{-1}$)	v_{rpl} ($m\,s^{-1}$)	t_f (μs)	El_f (–)	CPU (h)	w_m (mm)	T_m (K)	$K_{fp}+W_p$ (Nm)	$K_{fl}+W_l$ (Nm)	$K_{fg}+W_g$ (Nm)
Run 298-80 ($v_i=298.0\ m\,s^{-1}$)										
M1	243.7	270	28.0	96	14.2	1.99	1031	5874 + 570	792 + 775	72 + 527
M2	245.0	291	29.5	109	15.6	2.06	930	5938 + 587	770 + 828	79 + 528
M3	241.8	280	31.0	100	14.6	2.54	293	5783 + 589	725 + 916	101 + 611
M4	243.4	248	35.0	115	10.0	2.76	293	5865 + 526	575 + 983	111 + 634
M5	249.2	279	32.5	113	6.5	1.93	293	6147 + 526	665 + 839	70 + 474
M6	259.2	301	24.5	250	3.6	1.08	293	6659 + 497	634 + 588	41 + 309
M7	245.9	280	32.5	111	12.8	2.17	629	5983 + 573	688 + 875	84 + 507
Run 250-80 ($v_i=250.8\ m\,s^{-1}$)										
M1	199.7	238	30.4	93	17.8	2.54	951	3948 + 403	547 + 636	67 + 484
M2	198.7	226	33.6	96	21.0	2.85	854	3912 + 391	467 + 718	76 + 519
M3	190.8	222	46.8	103	25.2	4.75	293	3606 + 375	438 + 848	108 + 690
M4	181.5	221	60.5	132	17.4	5.18	293	3262 + 365	415 + 1022	159 + 803
M5	203.5	218	42.7	100	11.0	2.36	293	4104 + 353	418 + 701	60 + 437
M6	213.9	252	26.0	140	6.2	1.09	293	4535 + 352	500 + 455	34 + 243
M7	199.4	205	38.4	102	18.4	2.93	630	3942 + 386	367 + 781	81 + 504
Run 220-80 ($v_i=220.0\ m\,s^{-1}$)										
M3	147.4	185	58.0	105	32.1	5.90	293	2154 + 282	306 + 878	358 + 857
M4	133.2	154	76.0	134	23.5	7.96	293	1755 + 247	170 + 1041	275 + 1130
Run 191-80 ($v_i=190.7\ m\,s^{-1}$)										
M1	135.5	165	46.0	95	22.3	4.00	877	1824 + 197	244 + 550	100 + 556
M2	106.9	131	82.0	112	28.5	6.92	974	1121 + 200	144 + 839	255 + 894
M3	81.2[a]	–	100[b]	23	38.2	8.91	293	659 + 187	62 + 887	515 + 1221
M4	85.6[a]	–	100[b]	25	21.8	8.54	293	728 + 178	62 + 933	507 + 1133
M5	128.8	160	62.0	109	13.1	4.61	293	1646 + 177	227 + 710	119 + 579
M6	157.1	189	27.0	108	7.5	1.12	293	2452 + 180	323 + 334	33 + 189
M7	124.8	148	64.0	97	24.9	4.82	631	1545 + 195	208 + 725	141 + 641
M8	135.9	165	45.0	97	23.1	3.70	872	1834 + 197	244 + 546	110 + 537
Run 182-80 ($v_i=182.2\ m\,s^{-1}$)										
M1	115.9	146	60.0	99	25.9	4.34	830	1334 + 183	199 + 624	143 + 690
M2	99.9	120	81.0	105	31.5	6.72	729	989 + 181	136 + 758	244 + 841
M3	76.9[a]	–	100[b]	21	43.2	8.77	293	587 + 162	53 + 825	477 + 1123
M4	81.4[a]	–	100[b]	25	19.0	8.51	293	660 + 144	60 + 824	462 + 1067
M5	120.4	149	63.0	96	12.1	4.60	293	1438 + 154	196 + 672	121 + 574
M6	148.5	181	27.0	107	6.8	1.19	293	2191 + 160	299 + 321	34 + 190
M7	107.0	128	81.0	103	26.3	7.15	630	1134 + 176	155 + 755	196 + 725
Run 178-80 ($v_i=178.0\ m\,s^{-1}$)										
M2	84.8	98	100	104	34.1	7.09	793	713 + 154	77 + 815	275 + 975
M7	73.3	101	124	112	39.9	8.43	631	533 + 156	86 + 878	290 + 1033
Run 175-80 ($v_i=173.7\ m\,s^{-1}$)										
M1	104.4	126	86.0	99	29.9	5.10	881	1082 + 143	139 + 639	164 + 701
M2	77.8[a]	–	100[b]	43	34.0	7.24	815	600 + 142	55 + 813	381 + 921
M3	70.6[a]	–	100[b]	16	42.7	8.43	293	494 + 142	45 + 739	458 + 1060
M4	76.2[a]	–	100[b]	18	19.8	7.81	293	577 + 128	51 + 751	431 + 996
M5	94.7	122	88.0	126	12.2	6.06	293	891 + 144	124 + 750	231 + 712
M6	141.0	175	27.0	99	6.7	1.17	293	1976 + 145	274 + 300	34 + 176
M7	46.9[a]	–	150[c]	54	46.0	9.55	629	219 + 158	20 + 944	416 + 1151

Table 6 (*continued*)

Run #	v_r (m s^{-1})	v_{rpl} (m s^{-1})	t_f (μs)	El$_f$ (–)	CPU (h)	w_m (mm)	T_m (K)	$K_{fp} + W_p$ (Nm)	$K_{fl} + W_l$ (Nm)	$K_{fg} + W_g$ (Nm)
Run 165-80 ($v_i = 165.2$ m s^{-1})										
M1	84.2	107	87.0	98	33.9	6.93	770	703 + 134	107 + 627	170 + 839
Run 160-80 ($v_i = 160.0$ m s^{-1})										
M1	56.0	70	125	102	40.0	8.35	769	312 + 119	53 + 680	277 + 980
Run 156-80 ($v_i = 156.0$ m s^{-1})										
M1	34.1[a]	–	150[a]	27	44.8	9.08	781	116 + 108	11 + 641	386 + 1093

[a] No perforation at $t = t_{term}$.
[b] Termination time reached.
[c] Restarted with $t_{term} = 150$ μs.

arise compared with simulations using the coarse element mesh. First, the computational time is dramatically increased. The critical time step in LS-DYNA (1999) for quadrilateral elements is given as

$$\Delta t_e = \alpha \frac{L_s}{c_e} = \alpha \frac{A_s}{\max(L_i)} \sqrt{\frac{\rho(1+v)(1-2v)}{E(1-v)}} \tag{6}$$

where L_s is a characteristic length, A_s is the elements area, L_i $(i = 1, 2, 3, 4)$ is the length of the sides defining the element, c_e is the elastic wave speed in the material and α is a factor used to scale the critical time step for stability reasons in highly non-linear problems. During updating, the code determines the next time step by looping through all elements to determine the minimum value. This indicates that dividing all element sides by a factor 4 increases the computational time by a theoretical factor of $4^3 = 64$. However, since the elements are distorted during straining, this factor varies. The time steps for Run 230-20-M1 and Run 175-80-M1 are shown in Fig. 8. As seen, each time an element is removed from the mesh the time step is somewhat increased. Camacho and Ortiz (1997) discussed the use of eroding elements as opposed to adaptive remeshing. They concluded that both methods eliminate troublesome elements, but adaptive remeshing has the benefit of avoiding deformation-induced mesh disturbances, thus preventing the degradation of the time step required for stability. Similar results were obtained in a study using adaptive meshing by Børvik et al. (2000). Here, due to the steep gradients present in the problem it was found reasonable to scale the critical time step in order to increase the accuracy. Hence, the time steps in Fig. 8 are much smaller than the critical time step given by Eq. (6).

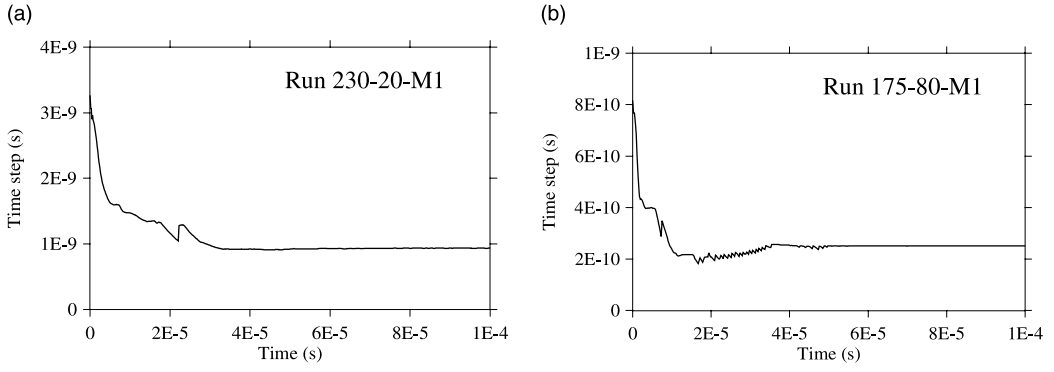

Fig. 8. Computational time step vs. time in Run 230-20-M1 and Run 175-80-M1.

The second effect is that a refined mesh will give a much better description of the localised behaviour. As shown in Fig. 5(b), this significantly improved the numerical results. Using the refined mesh, excellent agreement was obtained between the fully coupled damage model (M1) and the experimental data. The difference in ballistic limit was only 2% (see Table 5), and the ballistic limit curve of the target material was precisely determined. Also the results from the other models were improved. However, except for M5, which again showed a surprisingly close agreement with the experimental data, none of the other models were able to describe the experimentally obtained ballistic limit within 12%. For M3, M4 and M6 the deviation was more than 25%. As for the coarse element mesh, all models showed good agreement with the experimental data at the highest impact velocities. This illustrates the incorrectness of validating numerical simulations of plugging failure using experimental data at velocities well above the ballistic limit. When the details from the simulations in Table 6 were considered, similar observations as for the coarse mesh were obtained regarding local temperature, global target deformation, strain distribution, projectile perforation time and model efficiency. Again, M1 showed a better description of the perforation process than the other models.

The energy absorbed during penetration using the fine element mesh and model M1, M2 and M7 are shown in Fig. 7(b), and the behaviour was found somewhat different compared to the results using the coarse element mesh. At the highest impact velocities, about 42% of the energy was absorbed locally, 28% globally and 30% by the projectile using M1. As the impact velocity was reduced, more and more energy was absorbed in global target deformation, and at some point more energy was absorbed globally than locally. This distinct increase in global target deformation is as observed experimentally (see e.g. Fig. 2(b)). Close to the ballistic limit, approximately 55% of the energy was absorbed globally, 38% locally and 7% in projectile plastic deformation. About 1–3% of the energy was lost mainly due to removed elements (see Børvik et al., 2000). The energy absorbed by the projectile was found similar for both element meshes and all models, indicating that projectile deformation takes place early in the penetration process and is thus less sensitive to the target material model. However, while the plastic work carried out in the projectile at the lowest impact velocities seems reasonable, the amount of energy absorbed at the highest velocities seems high according to the literature. This is partly based on an analytical model by Johnson (1972) used to calculate the amount of energy necessary to plastically deform a linear strain hardening material from a cylinder into a frustum. Using the material input in Tables 1 and 3, the model indicates that less than 20% of the energy is used in projectile deformation. The reason for the discrepancy may be due to a too coarse element mesh in the projectile (see Fig. 16(a)), the omission of possible frictional effects between the projectile nose and target surface in the contact algorithm, or inaccuracies in the material data, material model or the numerical simulations itself.

In order to check the first two assumptions, some more simulations at the highest impact velocities were carried out. At first, a refined element mesh was used in the nose part of the projectile. A plot showing the deformed mesh 5 μs after impact in Run 298-80-M1 is given in Fig. 9. Such sudden refinements of the element mesh should be carried out with caution since reflections of stress waves may take place at the transition zone. However, the refined mesh did not affect the energy absorption in the different parts to any extent. Then, friction was added in the contact. According to Ravid and Bodner (1983), a frictional coefficient of 0.10 is usually given in the literature for dynamic metal working operations. This value was adopted in the simulations, even if a lower value was recommended in impact situations due to higher velocities and temperatures. Nor this attempt gave any change in the energy distribution. The plastic deformation of the projectile was also compared with the experimental observations. It was found that the change in projectile nose diameter (ΔD) was 0.7 mm and that the change in projectile length (ΔL) was 0.55 mm. These values are close to the measured values given in Table 1 for test 8–13. Thus, the energy absorbed by the projectile in the simulations seems to be reasonable. Of equal importance, the exercise reveals that projectile plastic deformation is an important parameter during structural impact, and cannot be neglected in calculations.

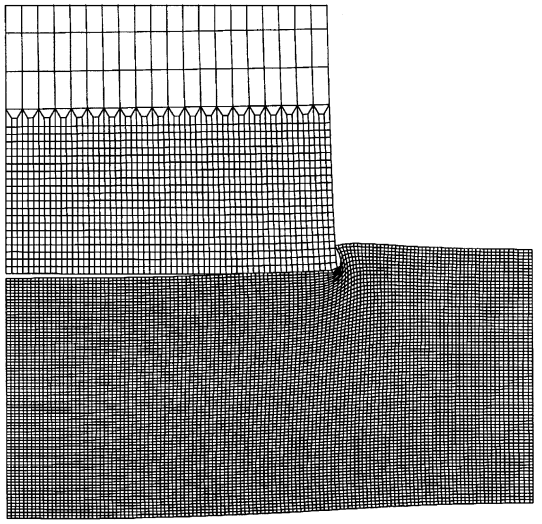

Fig. 9. Refined element mesh in the projectile 5 μs after impact in Run 298-80-M1.

4.4. Details from simulations

As shown, the element size is a vital parameter in numerical simulations involving localisation. Also, the fully coupled damage model (M1) was found superior to the other models in all simulations, even if the differences in ballistic limit velocity were not as distinct as first assumed. In order to demonstrate the features of the model, some details from simulations using M1 and the refined element mesh will be given in the following. Fig. 10 shows high-speed camera images from test 8–13 ($v_i = 298$ m s^{-1}) and test 8–8 ($v_i = 173.7$ m s^{-1}) compared with numerical results at identical times. The plots are shown as fringes of effective plastic strain, where "red" indicates a plastic strain above 30%. Not only are the residual velocity of the projectile and plug correctly predicted, but also the overall physical behaviour of the structure seems to be well described. This is further illustrated in Fig. 11, where the measured projectile velocity–time curves in Fig. 3 are compared with the numerical results. Again, excellent agreement is obtained between the experimental and numerical data. The final shape of the projectile and plug from test 8–8 are compared with the projectile and plug from Run 175-80-M1 in Fig. 12.

Details of the crack propagation and failure during perforation from Run 298-80-M1 is plotted as fringes of accumulated plastic strain in Fig. 13, while the number of failed elements as function of computational time for Run 298-80-M1 and Run 175-80-M1 are shown in Fig. 14. After the first indentation of the projectile, the critical damage is rapidly reached and a crack starts to grow. The crack propagates in front of the projectile towards the rear side of the target, and a plug is formed. If the plots in Fig. 13 are compared with metallurgical images of penetrated plates given in Børvik et al. (1999a), the behaviour is found very similar. As seen in Fig. 14, the number of failed elements is increased towards perforation. Close to fracture severe stretching appears in the localised zone. Since the failure strain is much more sensitive to tensile stresses than compression or shear (Børvik et al., 1999b), the fracture process is accelerated and a second crack starts to propagate from the rear side. When the two cracks meet, complete perforation appears and the plug is just pushed out of the cavity. This observation supports the general experimental assumption that the residual projectile velocity never is small, but a significant percentage of the initial velocity (Awerbuch and Bodner, 1974). Fig. 15(a) shows the difference in fracture patterns just above the ballistic limit using M1, M2 and M7, while Fig. 15(b) shows the fracture pattern from Run 175-80-M1. At

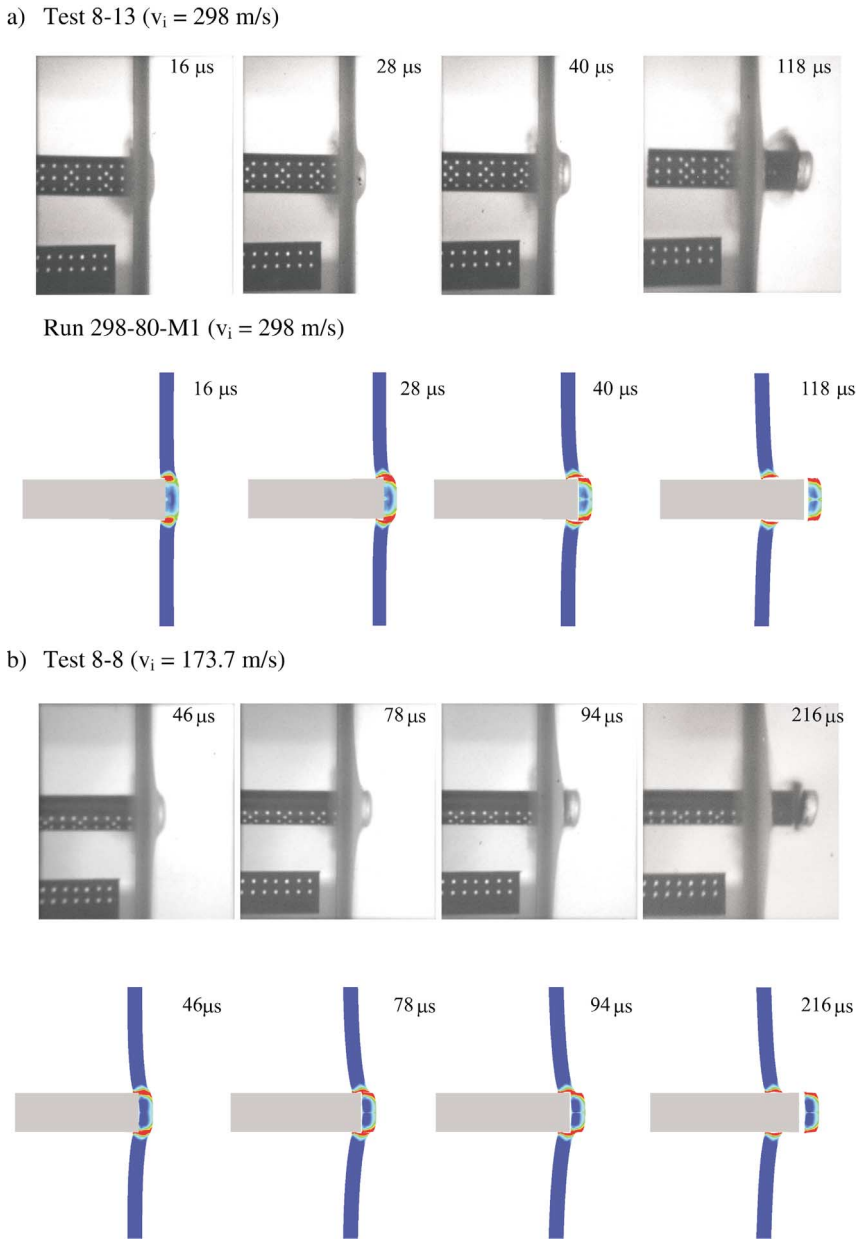

Fig. 10. High-speed camera images from test (a) 8–13 and (b) 8–8 compared to numerical simulations using model M1 with (a) coarse element mesh and (b) fine element mesh.

the highest impact velocities, most fracture patterns are similar to the one given in Fig. 15(c) from Run 298-80-M1, indicating grossly shear during perforation.

Fig. 16 shows details of the deformed element mesh and the distribution of equivalent von Mises stress, damage, stress triaxiality ratio, temperature and damaged plastic strain-rate in the target 63 μs after impact in Run 175-80-M1. These plots clearly illustrate that the deformation mainly develops in a narrow and

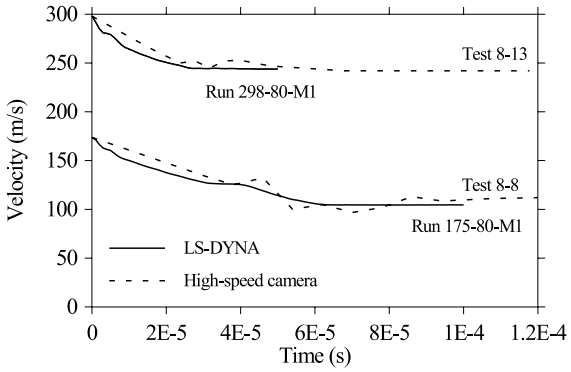

Fig. 11. Comparison between experimental and numerical velocity–time curves.

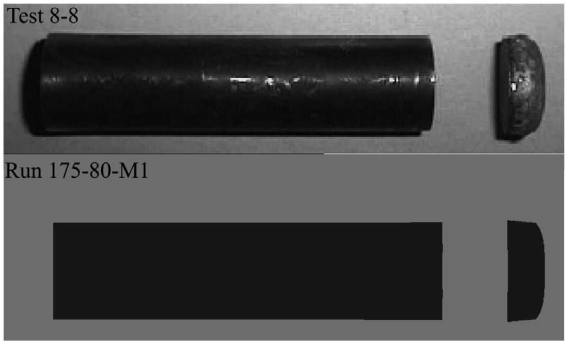

Fig. 12. Projectile and plug after perforation (test 8–8 and Run 175-80-M1).

almost vertical zone in the target. Outside the localised area, only small deformations are observed. Some details should be noticed. Due to bending, contact is occasionally reduced between the projectile and plug surface (see Fig. 16(a)). As a result, the interface force between the projectile and target is concentrated into a much smaller area near the sharp edge of the projectile. It should also be noticed that the material in front of the crack tip is severely damaged (Fig. 16(c)) and heated (Fig. 16(e)), causing a degradation of the material strength that facilitates fracture in that area. As indicated in Fig. 16(f), this is also the only area where the strain-rate is still high. The maximum damaged plastic strain-rate in the localised zone is found as high as $6 \times 10^5\ s^{-1}$. Finally, Fig. 16(d) shows the hydrostatic stress state in the target at this stage, indicating hydrostatic tension at the rear side of the target and in the localised shear zone, while the front is under severe hydrostatic compression. The stress state is found to change continuously during perforation, which again highly affects the fracture process.

The observations from Run 175-80-M1 are further outlined in Fig. 17, where the history variables included in the computational model are plotted for some of the elements. The position of the different elements in the mesh is shown in Fig. 6. All elements except element # 16 400 failed during impact. As seen, the behaviour of the elements is rather different and changes continuously depending on their location in the target. Roessig and Mason (1999) discussed the occurrence of adiabatic shear bands in punch test simulations. They concluded that even if some contradictions exist in the literature, a maximum stress criterion could be used as an indicator of whether adiabatic shear bands really occur or not. Roessig and

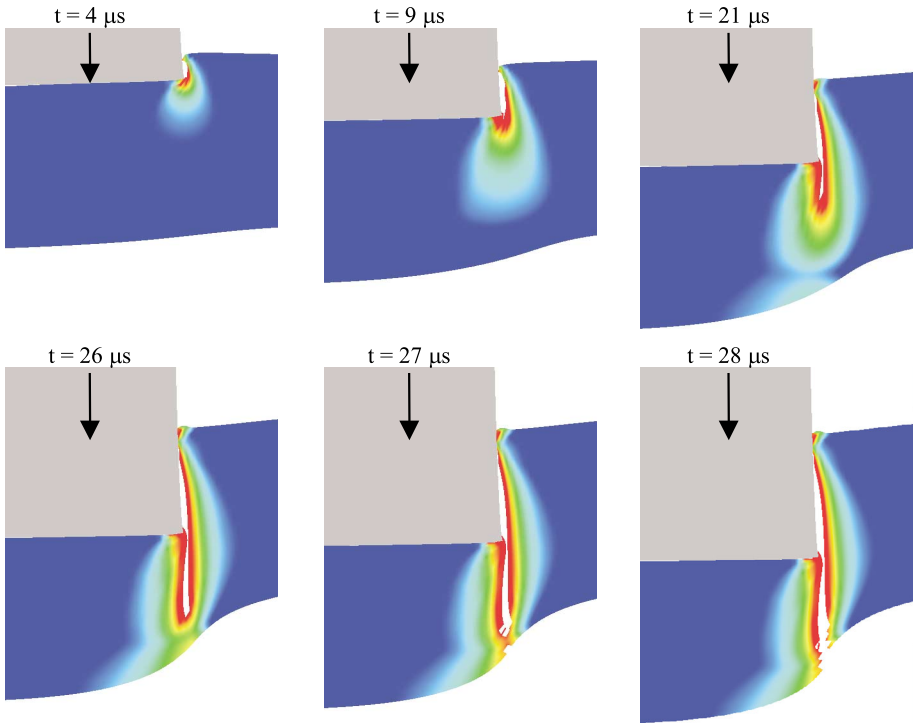

Fig. 13. Details of crack propagation and fracture in the target during penetration for Run 298-80-M1 (plotted as fringes of accumulated plastic strain).

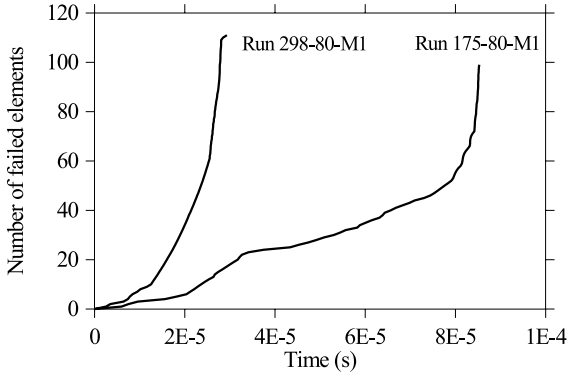

Fig. 14. Number of failed elements vs. time for Run 298-80-M1 and Run 175-80-M1.

Mason also showed that such a criterion is only valid if the change in strain and strain-rate with time is grater than or equal to zero, i.e. that the strain is a monotonically increasing function of time. Fig. 18(a) shows the effect on the equivalent stress in element # 19000 for each of the four different terms in Eq. (1). This element is located inside the proposed shear band. As seen, the strain hardening grows monotonically all the way to failure, while the strain-rate hardening gives a constant and positive contribution to the

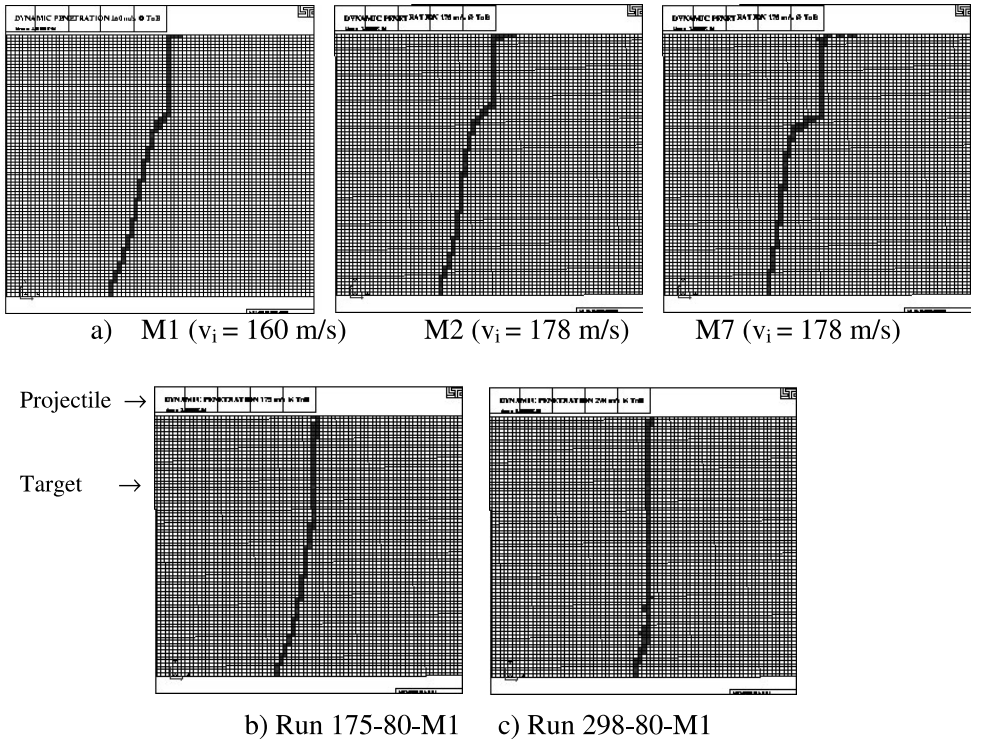

Fig. 15. Removed elements giving fracture patterns at (a) impact velocities just above the ballistic limit for M1, M2 and M7, (b) Run 175-80-M1 and (c) Run-298-M1.

equivalent stress. On the other side, the effect of material softening due to damage and temperature are found to be of equal importance and size. The effect of softening is moderate at first, but increases when the strain becomes large. When the effect of softening exceeds the effect of hardening, the equivalent stress starts to drop. This appears approximately 16 μs after impact. Since all criteria are satisfied, and all plots indicate a change in behaviour at this point, a true adiabatic shear localisation is assumed in the element. After localisation, the element is rapidly taken to failure.

Element # 16 400, which is located just outside the assumed shear band, shows a rather different behaviour. This is indicated in Fig. 18(b). At first, the behaviour is similar to the one observed in element # 19 000. After about 30 μs, a maximum is obtained in the stress–time curve, and the stress starts to drop. Simultaneously the effect of strain-rate decreases and approaches zero, while the accumulation of strain, damage and temperature stops. Thus, the drop in stress is not due to localisation, but is caused by unloading due to a loss in contact between the projectile and target. About 10 μs later contact is re-established and the history variables continues to grow toward a second maximum in the stress–time curve. Neither this point is due to localisation. Since the elements inside the proposed shear band now is localising, the area just outside the shear band is unloading. This can be seen since the strain-rate starts to decrease monotonically after about 45 μs, and that no more plastic strain is accumulated in the element. Since the accumulation of damage stops before the critical damage is reached, the element is not removed. All failed elements in this simulation are shown in the fracture pattern given in Fig. 15(b).

As just indicated the drop in equivalent stress observed in several of the elements after about 30 μs is not caused by localisation, but is due to unloading. At impact, the material in the plug is accelerated to a higher

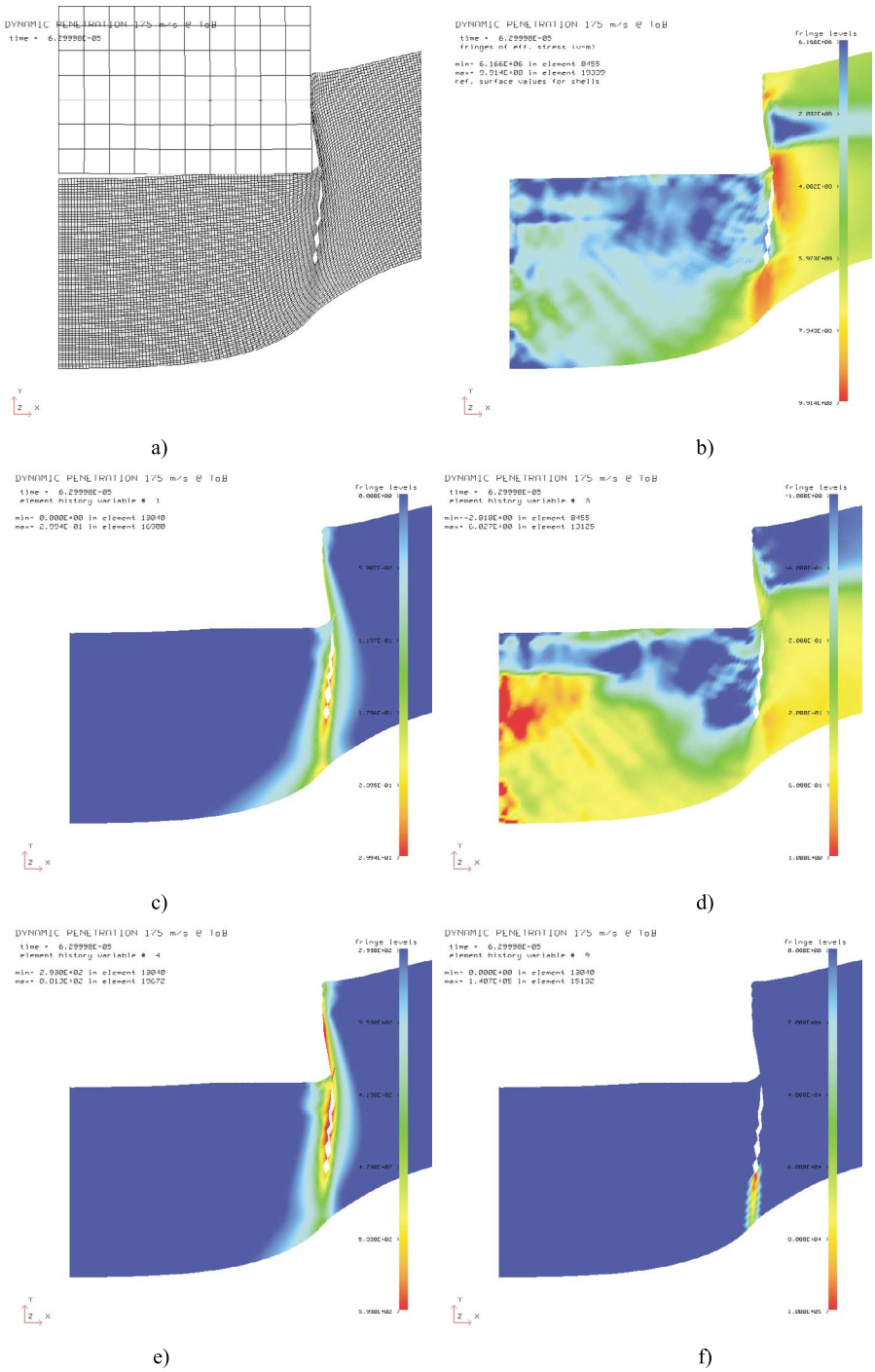

Fig. 16. (a) Deformed mesh and distribution of (b) equivalent von Mises stress, (c) damage, (d) stress triaxiality ratio, (e) temperature and (f) plastic strain-rate in the target 63 μs after impact in Run 175-80-M1.

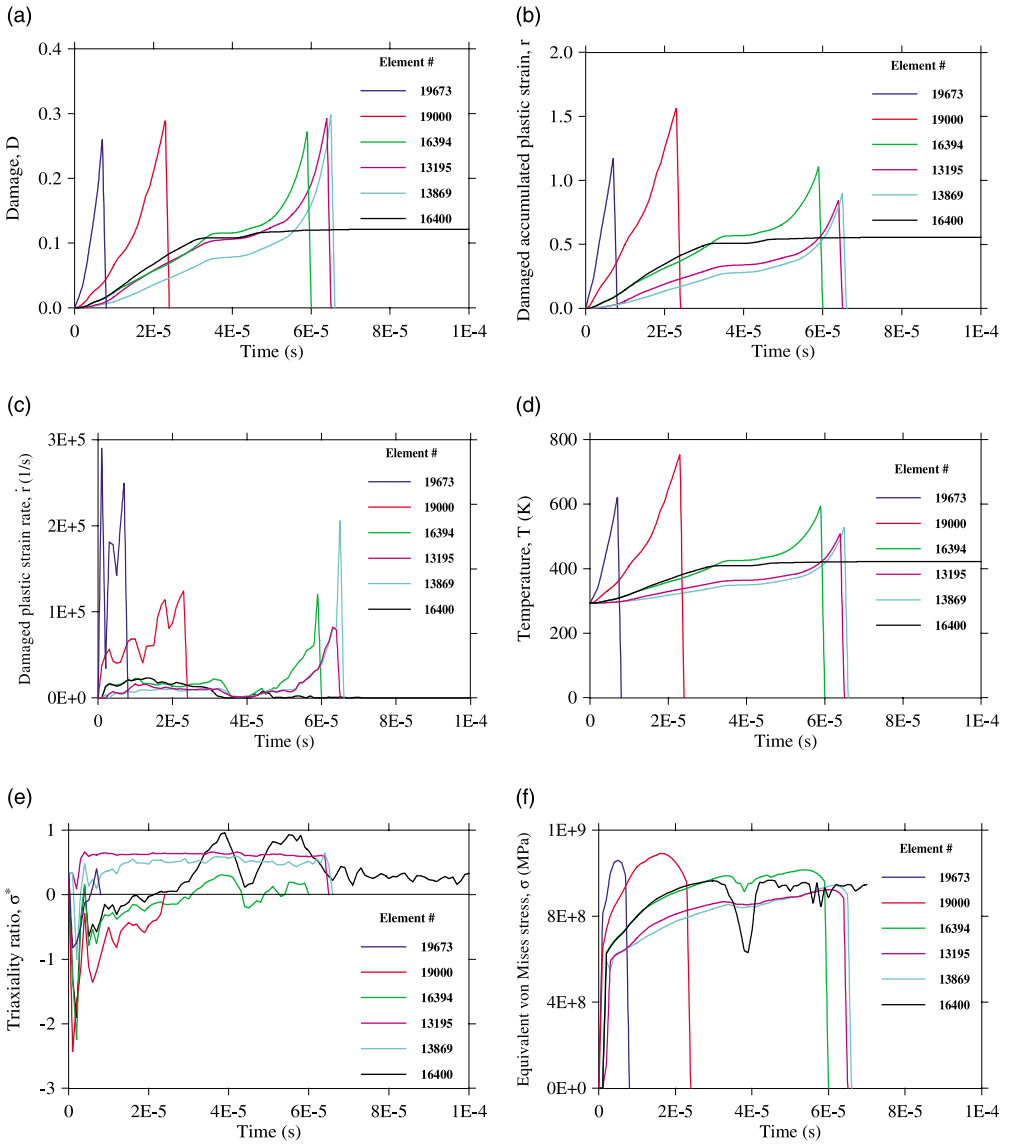

Fig. 17. Plots of some history variables for different elements as function of penetration time.

velocity than that of the projectile. Thus, contact between the projectile and plug is gradually lost and unloading occurs. However, due to restraining of the shear zone, the plug is prevented from leaving the target. The projectile catches up with the plug and full contact is re-established. This loss of contact during impact is seen both experimentally and numerically in the velocity–time plot in Fig. 10, and from the interface force–time plot in Fig. 19(a). As also shown in Fig. 19(b), this complete loss of contact is not seen in Run 298-80-M1. Several such impacts may take place during penetration. Close to or at perforation, this becomes an impact between two free bodies. This is believed responsible for the obtained difference in residual velocity between the projectile and plug.

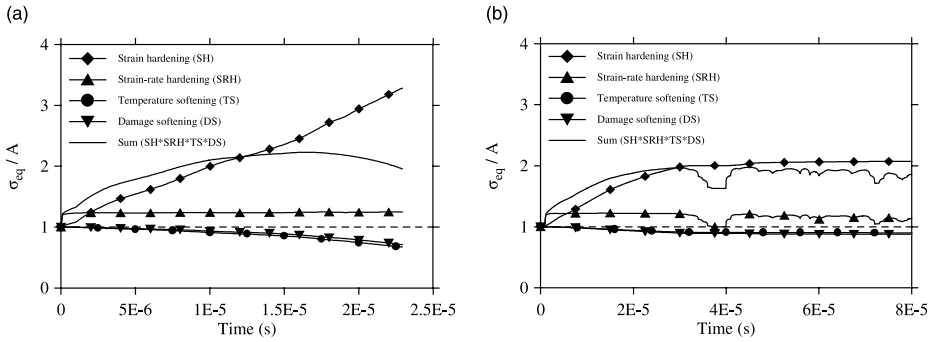

Fig. 18. The effect of strain hardening, strain-rate hardening, damage and temperature softening on the equivalent stress for element (a) 19 000 and (b) 16 400 in Run-175-80-M1. For comparison the equivalent stress is divided by the yield stress A of the target.

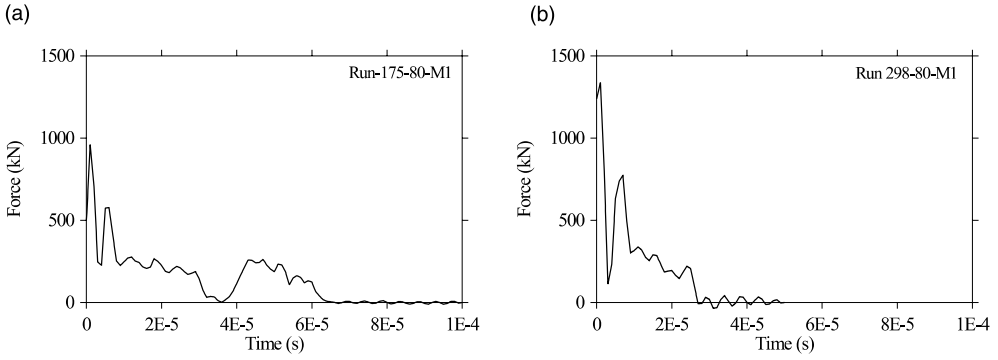

Fig. 19. Projectile force vs. penetration time in (a) Run 175-80-M1 and (b) Run 298-80-M1.

5. Concluding remarks

A coupled computational material model of viscoplasticity and ductile damage for projectile penetration has been developed and implemented in LS-DYNA (1999). In the present study, eight different complexity levels of the material model have been used in numerical simulations of plugging failure during ballistic penetration in order to investigate the importance of the constitutive relationship in the problem. The numerical results have been compared with observations from gas-gun experiments where blunt-nosed projectiles were launched against 8-mm thick Weldox 460 E steel plates. From the study, the following main conclusions can be drawn:

- The element size is found to be a vital parameter in numerical simulations involving adiabatic shear localisation. Since the width of the experimentally obtained shear zone is much smaller than the element size normally used, this is as expected. When a coarse element mesh was used, none of the models were able to predict the experimentally obtained ballistic limit within 30%. However, when the mesh was sufficiently refined the agreement was significantly improved.
- All models showed reasonable agreement with the experimental observations at impact velocities well above the ballistic limit. However, as the impact velocity approached the ballistic limit, the difference between the models was increased.

- Strain-rate, temperature and stress state were all found to be important parameters. If not included in the model, considerable errors could appear.
- The fully coupled computational model of viscoplasticity and ductile damage showed the best agreement with the experimental results in all simulations, but the difference in ballistic limit between M1, M2 and M7 was not significant. However, when details from the numerical simulations were compared, important and distinct differences were obtained.
- Examples from simulations using M1 showed that details like energy absorption, crack propagation, fracture patterns, strain localisation and overall physical behaviour were well predicted by the model.
- The detailed insight into the behaviour of penetrated steel plates obtained using the computational model of viscoplasticity and ductile damage is hard, if possible at all, to get from experimental tests or analytical calculations. Thus, numerical simulations using a verified and validated material model seem to be an essential tool in order to increase the physical understanding of the different processes in structural impact.
- Finally, an important issue in numerical simulations of structural impact that has not been discussed in this paper is related to contact algorithms and adaptive meshing. Even if the methods used in this study seems to work satisfactory in plugging failure, this may not be the case in e.g. ductile hole enlargement using conical projectiles. Here, adaptive meshing may become necessary. However, adaptivity introduces new challenges and variables not present when a homogeneous element mesh is used.

Acknowledgements

The authors would like to acknowledge the Norwegian Defence Construction Service, Central Staff/ Technical Division, Oslo, Norway, for their support of this work.

References

Awerbuch, J., Bodner, S.R., 1974. Experimental investigation of normal perforation of projectiles in metallic plates. Int. J. Solids Struct. 10, 685–699.

Bai, Y., Dodd, B., 1992. Adiabatic Shear Localisation. Pergamon Press, New York.

Bammann, D.J., Chiesa, M.L., Horstemeyer, M.F., Weingarten, L.I., 1993. Failure in ductile materials using finite element simulations. In: Jones, N., Wierzbicki, T. (Eds.), Structural Crashworthiness and Failure. Elsevier, Amsterdam, pp. 1–54.

Batra, R.C., Peng, Z., 1996. Development of shear bands during the perforation of a steel plate. Comput. Mech. 17, 326–334.

Belytschko, T., 1996. On difficulty levels in non linear finite element analysis of solids. Bull. Int. Assoc. Comput. Mech. 2, 6–8.

Berstad, T., Hopperstad, O.S., Langseth, M., 1994. Elasto-Viscoplastic Constitutive Models in the Explicit Finite Element Code LS-DYNA3D. Proceedings of Second International LS-DYNA3D Conference, San Francisco, 20–21 September.

Børvik, T., Holen, K., Langseth, M., Malo, K.A., 1998a. An Experimental set-up used in Ballistic Penetration. Proceedings Fifth International Symposium Structures under Shock Impact, Thessaloniki, Greece, 24–26 June pp. 683–692.

Børvik, T., Langseth, M., Hopperstad, O.S., Malo, K.A., 1998b. Penetration of Steel Plates- I. Experimental Study. Proceedings Third International Symposium Impact Engng. Oxford University Press, Singapore, 7–9 December.

Børvik, T., Langseth, M., Hopperstad, O.S., Malo, K.A., 1999a. Ballistic penetration of steel plates. Int. J. Impact Engng. 22 (9–10), 855–887.

Børvik, T., Hopperstad, O.S., Berstad, T., Langseth, M., 1999b. Computational Model of Viscoplasticity and Ductile Damage for Projectile impact. submitted for publication.

Børvik, T., Hopperstad, O.S., Berstad, T., Malo, K.A., Langseth, M., 1999c. Numerical Simulation of Plugging Failure in Ballistic Penetration using LS-DYNA, Proceedings Second European LS-DYNA User Conference, Gothenburg, Sweden, 14–15 June.

Børvik, T., Hopperstad, O.S., Berstad T., Langseth, M., 2000. Effect of Projectile Nose Shape in Structural Impact, Part II: Numerical Simulations. submitted for publication.

Camacho, G.T., Ortiz, M., 1997. Adaptive Lagrangian modelling of ballistic penetration of metallic targets. Comp. Meth. Appl. Mech. Engng. 142, 269–301.

Chen, E.P., 1992. Numerical simulation of shear induced plugging in HY100 steel plates. Int. J. Damage Mech. 1, 132–143.

Chou, P.C., Hashemi, J., Chou, A., Rogers, H.C., 1991. Experimentation and finite element simulation of adiabatic shear bands in controlled penetration impact. Int. J. Impact Engng. 11, 305–321.

Harding, J., 1989. The development of constitutive relationships for material behaviour at high rates of strain. Int. Conf. Mech. Prop. Materials at High Rates of Strain, Oxford.

Hopperstad, O.S., Børvik, T., Berstad, T., Aas-Jakobsen, K., Langseth, M., 1998. Penetration of Steel Plates-II. Numerical Simulations. Proceedings Third International Symposium Impact Engng., Singapore, 7–9 December.

Johnson, G.R., Cook, W.H., 1983. A Constitutive Model and Data for Metals Subjected to Large Strains, High Strain Rates and High Temperatures. Seventh International Symposium Ballistics, The Hague, The Netherlands, pp. 541–547.

Johnson, G.R., Cook, W.H., 1985. Fracture characteristics of three metals subjected to various strains, strain rates and temperatures. Engng. Fract. Mech. 21, 31–48.

Johnson, W., 1972. Impact Strength of Materials. Edward Arnold Ltd, London.

Le Roy, G., Emburt, J.D., Edward, G., Ashby, M.F., 1981. A model of ductile fracture based on the nucleation and growth of voids. Acta Metall. 29, 1509–1522.

Lemaitre, J., 1992. A Course on Damage Mechanics. Springer, Berlin.

LS-DYNA, 1999. LS-DYNA User's Manual, Version 950.

Needleman, A., 1988. Material rate dependence and mesh sensitivity in localisation problems. Comp. Meth. Appl. Mech. Engng. 67, 69–85.

Ravid, M., Bodner, S.R., 1983. Dynamic perforation of viscoplastic plates by rigid projectiles. Int. J. Impact Engng. 21 (6), 577–591.

Recht, R.F., Ipson, T.W., 1963. Ballistic perforation dynamics. Int. J. Appl. Mech. Trans. ASME 30, 384–390.

Roessig, K.M., Mason, J.J., 1999. Adiabatic shear localisation in the dynamic punch test, part II: numerical simulations. Int. J. Plasticity 15, 263–283.

Wen, H.-M., Jones, N., 1996. Low-velocity perforation of punch-impact-loaded metal plates. Trans. ASME J. Press. Vessel Technol. 118, 181–187.

Zerilli, F.J., Armstrong, R.W., 1987. Dislocation-mechanics-based constitutive relations for material dynamic calculations. Int. J. Appl. Phys. 65, 1816–1825.

Zukas, J.A. (Ed.), 1990. High Velocity Impact Dynamics. Wiley, New York.